arXiv:1611.07666v1 [cond-mat.mtrl-sci] 23 Nov 2016

X-ray dynamical diffraction in amino acid crystals: a step towards improving structural resolution of biological molecules via physical phase measurements

Sérgio L. Morelhão*
Institute of Physics, University of São Paulo, São Paulo, SP, Brazil

Cláudio M. R. Remédios
Faculdade de Física, Universidade Federal do Pará, Belém, PA, Brazil

Guilherme Calligaris
Instituto de Física, Universidade Estadual de Campinas, Campinas, SP, Brazil

Gareth Nisbet
Diamond Light Source, Harwell Science and Innovation Campus, OX11 0DE, UK

(Dated: November 24, 2016)

In this work, experimental and data analysis procedures were developed and applied for studying amino acid crystals by means of X-ray phase measurements. It clearly demonstrated the sensitivity of triplet phases to electronic charge distribution responsible for intermolecular forces in D-alanine crystal. Phase measurement from multiple diffraction provides a complementary information to that provided by nuclear methods such as neutron diffraction and nuclear magnetic resonance.

I. INTRODUCTION

From inorganic crystals to protein crystals, structure determination with atomic resolution is mostly based on diffraction techniques (electrons, X-rays, and neutrons). However, since the coherent scattering cross-section for X-ray by atoms have intermediate values between those for electrons and neutrons, experimental measurements of structure factor phases have been successfully carried out with X-rays[1]. Dynamical diffraction taking place within perfect domains is another requirement for physical phase measurements via multiple diffraction (MD) experiments. In crystals with small unit cells, dynamical diffraction regime is achieved in much smaller domains than in crystals with large cells such as protein crystals. Fact that has allowed phase measurements to reveal structural details—inaccessible by other techniques—in optical crystals with dopant ions[1,2], as well as to solve chirality in crystals with no resonant atoms[3].

In this work, we first present a simple approach to graphical indexing of appropriate cases for phase measurements, e.g. Fig. 1 (bottom panel), which is also very useful for other diffraction techniques in semiconductor devices and single crystals in general[4,5]. Then, we present diffraction data in single crystals of D-alanine carried out at two synchrotron facilities and with different instrumentation (flux, optics, and goniometry). Model structures taking into account ionic charges are proposed and compared to experimental data, leading to an ideal model to describe X-ray diffraction by this simple amino acid molecule in terms of invariant phase triplets.

II. MODEL STRUCTURES

Since 6 performed the first azimuthal scanning in the early 20th century, the so called Renninger scanning, excitation of 2nd-order diffractions, MDs for short, and their potential applications in X-ray crystallography have been investigated. Every time similar experiments are carried out, very often the intensity profiles exhibit characteristic asymmetries, such as those seen in Fig. 1 (top panel), owing to dynamical coupling of the simultaneously diffracted waves inside a single crystal domain. Over several decades, these often observed asymmetries have motivated numerous researches in developing theoretical approaches and experimental procedures to process MD intensity profiles into structural information[7–14].

Recently it has been realized that the only reliable information is the type of asymmetry, i.e. if the asymmetry has lower/higher (L|H) or higher/lower (H|L) shoulders[3]. It implies in new strategies on how to look at these asymmetries. To demonstrate in practice one of such strategies, we choose the challenge of detecting hydrogen bonding charges responsible for intermolecular forces between amino acid molecules. It is a critical bond in life science, stabilizing the structures of proteins and zipping together the DNA double helix. Therefore, an X-ray based method to study this type of chemical bond is an important advance in terms of structural analysis, offering information on electronic charges to complete the usual data from nuclear methods.

With molecular formula $C_3H_7NO_2$, D-alanine is the smallest molecule among the amino acids. When grown in aqueous solution, it crystallizes in space group $P2_12_12_1$ at ambient pressure, with four molecules per unit cell. Intermolecular forces are hydrogen bonds where the amino group of each molecule makes N–H$\cdots$O bonds with three other molecules[15,16], Fig. 2, or van der Waals forces be-

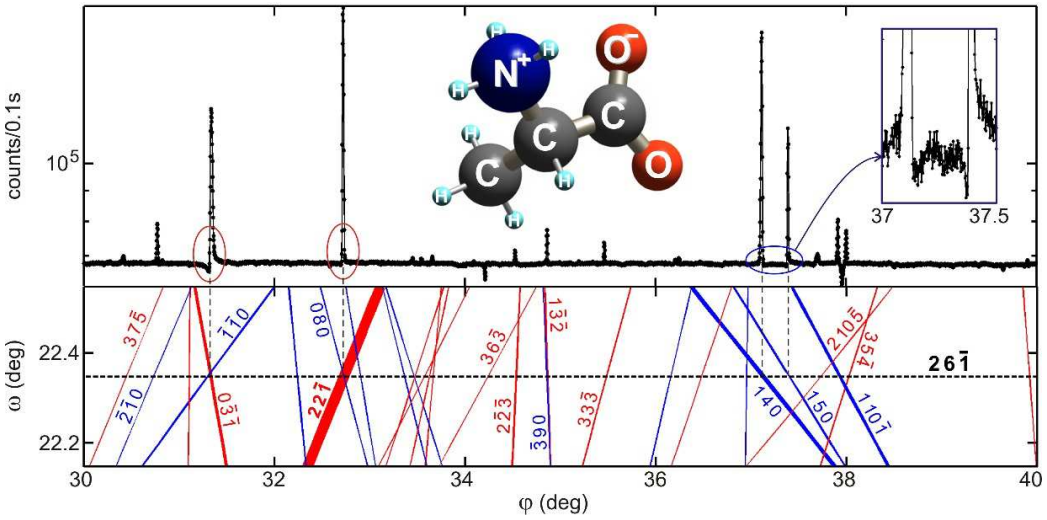

FIG. 1: Dynamical diffraction in D-alanine crystal giving rise to asymmetric intensity profiles in MD cases (top panel). X-rays of 10 keV, σ polarization. Inset: zwitterion of D-alanine. Graphical indexing through Bragg-cone lines (bottom panel) provides a general picture of the nearby cases, their relative strength (line thickness), and easy distinction of the out-in/in-out geometries (blue/red lines). MD peaks are seen at the intersections of Bragg-cone lines with the $26\bar{1}$ one (horizontal dashed line).

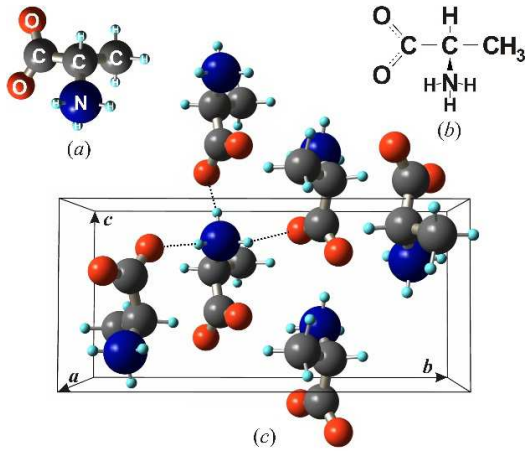

FIG. 2: (a,b) D-alanine molecule, 3D and plain view. (c) NH$\cdots$O bonds (dashed lines) between adjacent molecules in the crystal structure, orthorhombic unit cell of lattice parameters $a = 6.031(3)$ Å, $b = 12.335(5)$ Å, and $c = 5.781(3)$ Å.

tween zwitterions[17]. In either cases, there is a non-spherosymmetric electronic charge distribution at the amino group. X-ray sensitivity to this charge distribution can be verified by comparing diffraction data from two model structures. In one model, tagged as the NH3 model, hydrogen atoms are set around the nitrogens at distances of 1.05 ± 0.02 Å, Fig. 2(a), as determined by neutron diffraction[18]. In the other model, tagged as the N3e model, hydrogen electrons are placed in the nitrogen orbitals so that the amino groups scatter X-rays as the N^{3-} ion with spherosymmetric charge distribution.

Simulated X-ray powder diffraction patterns for both model structures are compared in Fig. 3. It shows that to distinguish between these models, experimental accuracy better than 1% (regarding the main peak) in measuring relative intensities of diffraction peaks is required. Tabulated[19] atomic scattering factors for neutral atoms were used in calculating diffracted intensities of the NH3 model structure, while the atomic scattering factor of the N^{3-} ion[3] stands for the whole scattering of amino groups in the N3e model.

III. INTRODUCTION TO PHASE MEASUREMENTS

Phase measurement is based on the fact that in a crystal undergoing dynamical diffraction, the integrated intensity of one reflection, reflection G, when measured as a function of the excitement of another reflection, reflection H, gives rise to an intensity profile whose asymmetry depends on the invariant phase triplet[11]

$$\Psi = \delta_H + \delta_{G-H} - \delta_G \qquad (1)$$

where δ_X is the phase of structure factor F_X of reflection X ($X = G$, H, and $G - H$).

Therefore, to identify the best diffraction model for this amino acid crystal based on phase measurements, it is necessary first to search for structure factors with phases susceptible to changes in the models, as done in Fig. 4(a). It indicates a few reflections, such as 202, 252, and 261, that are good candidates for phase measurements. Since these reflections have small $|F_G|$ values, i.e. are weak reflections, they can only be used as the primary G reflection. After selecting one reflection, the next step is to figure out secondary H reflections that promote MD cases with opposite profile asymmetries for each proposed

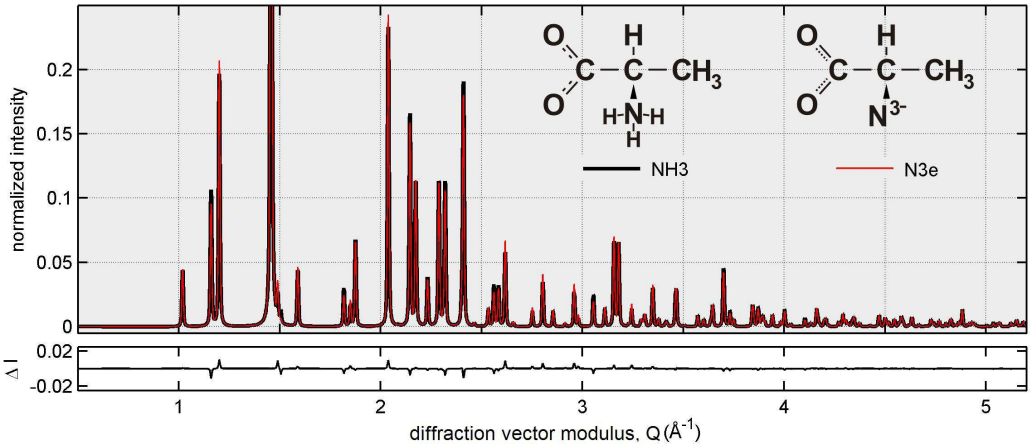

FIG. 3: Comparison of simulated XRD patterns according to NH3 and N3e model structures. X-rays of 10 keV, σ polarization.

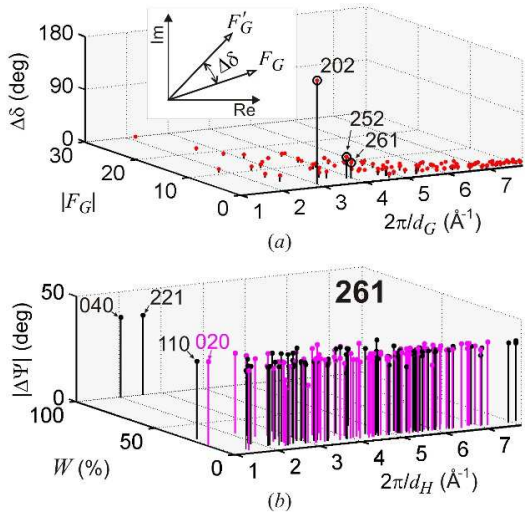

FIG. 4: (a) Difference $\Delta\delta$ in structure factor phases regarding the proposed models, as detailed in the inset (NH3$\rightarrow F_G$ and N3$e \rightarrow F'_G$). X-rays of 10 keV. (b) Three-beam cases predicted to show opposite profile asymmetries on each model structure according to the criteria $\cos(\Psi)\cos(\Psi') < 1$. $G = 261$ and $\Delta\Psi = \Psi' - \Psi$ (NH3$\rightarrow \Psi$ and N3$e \rightarrow \Psi'$). Limited to amplitude $W > 5\,\%$. $d_{G,H}$ is the interplanar distance of Bragg planes.

model structures. It can be done by calculating

$$F_H F_{G-H}/F_G = W e^{i\Psi} \tag{2}$$

for both models and picking up the cases where the phase shift $\Delta\Psi$ is large enough to make the phase triplet crossing the $\pm 90°$ values, i.e. those cases where $\cos(\Psi)\cos(\Psi+\Delta\Psi) < 1$. A graphical example of this procedure is given in Fig. 4(b) for 261 as the G reflection. It foresees many cases having opposite asymmetries, including the cases for the 221 and 040 secondary reflections with the largest relative values of the amplitude W (see detailed list in §A 3).

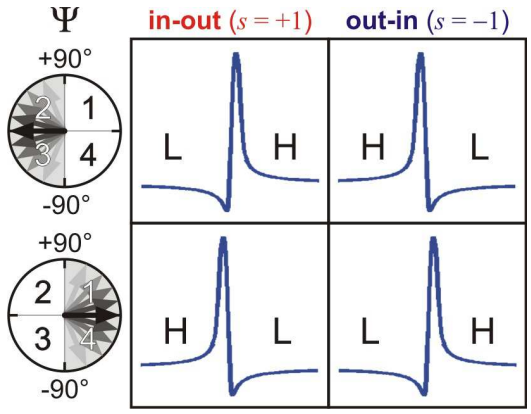

FIG. 5: Criteria of H|L ($s\cos(\Psi) > 1$) or L|H ($s\cos(\Psi) < 1$) profile asymmetry in three-beam diffraction with respect to the in-out ($s = +1$) or out-in ($s = -1$) geometry of excitement and interval of values of the phase triplet Ψ: $\cos(\Psi) < 1$, quadrants 2 and 3 (top panels), or $\cos(\Psi) > 1$, quadrants 1 and 4 (bottom panels).

IV. GRAPHICAL INDEXING OF RENNINGER SCANS

For any reflection of diffraction vector $\boldsymbol{Q}$, a two-dimensional representation of its Bragg cone (BC) is given by the relationship[4]

$$\cos(\varphi - \alpha_Q) = \frac{\sin\theta - \sin\omega\,\cos\gamma_Q}{\cos\omega\,\sin\gamma_Q}\,. \tag{3}$$

ω and φ are the instrumental angles describing the incident wavevector

$$\boldsymbol{k} = -\frac{2\pi}{\lambda}[\cos\omega\,\cos\varphi,\ \cos\omega\,\sin\varphi,\ \sin\omega]$$

on a sample xyz frame where z is along the azimuthal rotation axis. The α_Q and γ_Q angles are obtained by projecting the diffraction vector on this crystal frame,

i.e.,

$$\boldsymbol{Q} = |\boldsymbol{Q}| \left[\sin\gamma_Q \cos\alpha_Q,\, \sin\gamma_Q \sin\alpha_Q,\, \cos\gamma_Q\right],$$

$|\boldsymbol{Q}| = (4\pi/\lambda)\sin\theta$, and $\boldsymbol{k}\cdot\boldsymbol{Q} = -|\boldsymbol{Q}^2|/2$.

Eq. (3) provides two solutions for the azimuth φ as a function of the incidence angle ω. These solutions represent the two possible excitation geometries that are plotted as the out-in (blue) and in-out (red) BC lines in the $\omega:\varphi$ graphs, e.g. Fig. 1. Using lines of different colors to identify each one of these solutions is quite helpful since the observed profile asymmetries depend on both phase and excitation geometry, as summarized in Fig. 5. Another useful trick for graphically indexing Renninger scans is plotting BC lines with relative thickness. Here we use line thicknesses proportional to the amplitude W, Eq. (2). For instance, in the Renninger scan of reflection $26\bar{1}$ in Fig. 1, the strongest peak has the thickest BC lines due to secondary $22\bar{1}$ reflection.

V. EXPERIMENTAL

Single crystals of D-alanine were grown by slow evaporation from supersaturated aqueous solutions: D-alanine powder (98% purity) diluted in distilled water, concentration of 0.25 g/ml, and pH between 6 and 6.5. The solution was kept at a constant temperature (296K) in a beaker covered with perforated plastic lid during three weeks. Transparent single crystals showing well-formed natural faces were obtained, such as the one used here with approximated dimensions of $4\times3\times10\,\mathrm{mm}^3$ and largest face as the (130) planes (§A 1, Fig. 11). Lattice parameters $a = 6.031(3)$ Å, $b = 12.335(5)$ Å, and $c = 5.781(3)$ Å were determined by X-ray powder diffraction in another sample of the same batch, and they agree very well with the MD peak positions within an accuracy of 0.01°.

X-ray data acquisition were carried out at the Brazilian Synchrotron Light Laboratory (LNLS), beamline XRD2, and at the Diamond Light Source, beamline I16, testing advantages and limitations of two possible procedures for measuring line profiles of MD peaks. In one procedure, both adjustment arcs of the goniometric head are used to physically align the primary diffraction vector with one rotation axis of the sample stage. Wide azimuthal scans are possible, although eventual corrections of the incidence angle are necessary depending on the residual misalignment between the diffraction vector and the rotation axis. This procedure is preferred in term of accuracy in both line profile and position of the peaks[20]. But, after fixing the sample, it is limited to reflections that can be aligned within the ±20° range of the adjustment arcs. Rotating crystal method for indexing and pre-alignment of accessible reflections have been used, as demonstrated in §A 2.

In the other procedure, the azimuthal scans are performed by combining rotations of the diffractometer axes. This multi-axis goniometry is the standard procedure in single crystal diffractometers. The sample is fixed at the holder within eye accuracy and after finding two non parallel reflections, the crystal orientation matrix is built. With a proper script for azimuthal scanning, it is possible to inspect many primary reflections automatically. But, the number of accessible MD cases and data accuracy depend on angular range of combined rotations and sphere of confusion of the used diffractometer.

Despite of the distinct instrumentations at the used beamlines, energy and angular resolution were nearly the same: spectral width of 2×10^{-4} and beam divergences of 0.1 mrad. Brightness of the beam at I16 have required some attention to avoid fast radiation damage to fragile crystals with van der Waals bonds such as D-alanine. Exposure to the direct beam cause immediate damage, e.g. the streaks seen at the (130) surface in Fig. 11 (inset). Primary $26\bar{1}$ was measured with the physical alignment procedure and X-rays of 10 keV, while the multi-axis goniometry was used to measure a few MD cases with primaries 261 and 080, and X-rays of 8 keV. Vertical scattering plane (σ polarization) has been used in all measurements where the asymmetry criteria in Fig. 5 apply for most MD cases. For other polarizations these criteria must be reviewed[13,21,22].

H	Ψ (°)	Ψ' (°)	W(%)	R_a	φ_0 (°)
$37\bar{5}$r	65	104	6	2.2 (H|L)	30.415
$2\bar{1}0$b	−111	−74	9	2.2 (H|L)	30.773
$0\bar{3}\bar{1}$r	165	−158	29	−33.8 (L|H)	31.341
$\bar{1}\bar{1}0$b	−3	31	16	— —	31.341
$22\bar{1}$r	−98	−60	100	−12.6 (L|H)	32.722
080b	69	106	7	— —	32.722
$2\bar{2}\bar{3}$r	73	108	11	1.0 (H|L)	34.527
$1\bar{3}\bar{2}$r	0	31	12	3.7 (H|L)	34.863
$\bar{3}90$b	−111	−72	6	— —	34.863
$33\bar{3}$r	−116	−72	11	−1.1 (L|H)	35.463
140b	100	143	38	32.8 (H|L)	37.114
150b	−3	32	16	−11.5 (L|H)	37.391

TABLE I: Theoretical triplet phases according to structure models NH_3 (Ψ) and N3e (Ψ') of D-alanine for a few secondary H reflections seen in Fig. 1 where b/r letters stand for blue/red BC lines. Experimental peak asymmetries are given in terms of parameter R_a, Eq. (4). Relative amplitudes and positions are estimated by W and φ_0 values, respectively.

VI. RESULTS AND DISCUSSIONS

Line profile asymmetries have been determined according to the value of

$$R_a = 2\left(\Delta I_L - \Delta I_R\right)/\sqrt{\min\{I_s\}} \qquad (4)$$

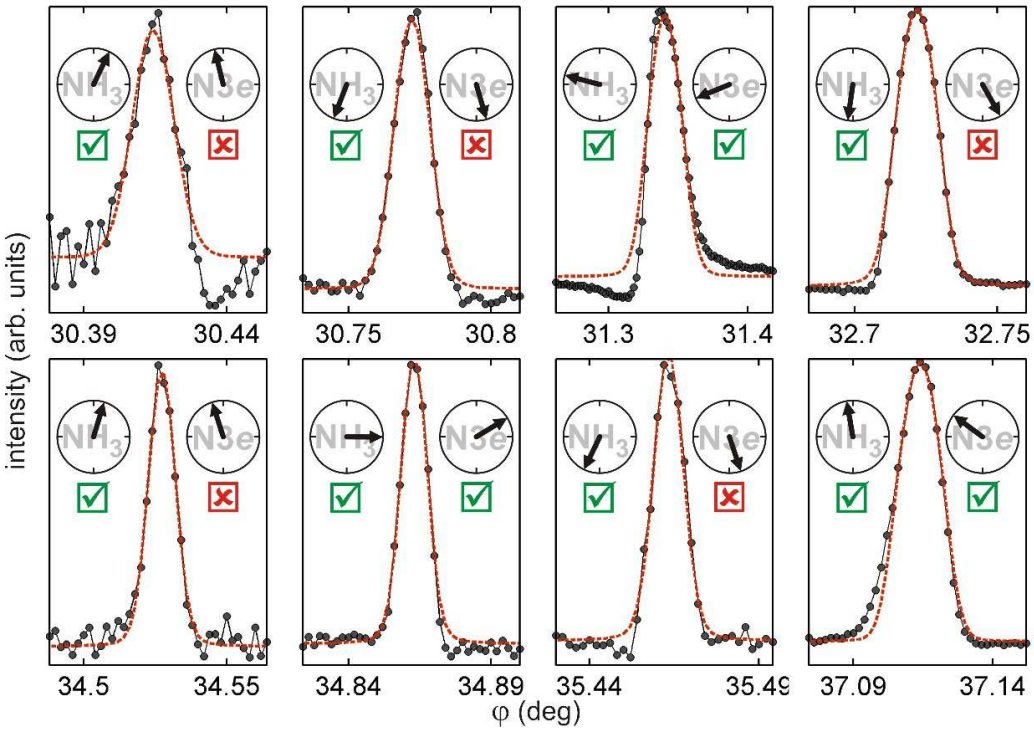

FIG. 6: Experimental intensity profiles (closed circles connected by lines) of multi-beam diffraction in D-alanine shown against data fitting (dashed-red lines) with a symmetrical function. Phase values of each model structure and their compatibility (checkbox) with the observed profile asymmetries are indicated aside of each peak.

where

$$\Delta I_L = \frac{1}{N_{\varphi_j<\varphi_0}} \sum_{\varphi_j<\varphi_0} [I_e(\varphi_j) - I_s(\varphi_j)]$$

and

$$\Delta I_R = \frac{1}{N_{\varphi>\varphi_0}} \sum_{\varphi_j>\varphi_0} [I_e(\varphi_j) - I_s(\varphi_j)] \,.$$

$N_{\varphi_j<\varphi_0}$ and $N_{\varphi_j>\varphi_0}$ are the number of data points at the left and right side of the diffraction peak, respectively. $\Delta I_{L,R}$ stand for the mean intensity difference on each side of the peak since $I_e(\varphi_j)$ is the jth experimental data point and $I_s(\varphi_j)$ is the corresponding point obtained by data fitting with a symmetric pseudo-Voigh function, which also provides the peak center φ_0. The asymmetric character of each intensity profile is therefore given as H|L when $R_a \geq 1$ or L|H when $R_a \leq -1$. Diffraction peaks are considered symmetric, i.e. with an indistinguishable type of asymmetry, when $|R_a| < 1$. A few examples of data fitting by symmetric line profile function are shown in Fig. 6, and the corresponding R_a values given in Table I.

Compatibility analysis between experimental asymmetries and proposed models is carried out on bases of a true/false test according to

$$s\cos(\Psi)R_a \begin{cases} > 1 \;\Rightarrow\; \text{true} \\ < 1 \;\Rightarrow\; \text{false} \end{cases} , \qquad (5)$$

which is reliable as far as $|R_a| \geq 1$. The true/false outcomes for each model are indicated at checkboxes aside each experimental profile in Fig. 6.

Beyond the few cases shown in Fig. 6, all experimental profiles observed in the complete Renninger scan of the $26\bar{1}$ reflection (see §A 1) were consistent with the NH3 model or with a refined version of this model, as discussed later. Even profiles that are in the symmetric/asymmetric limit where $|R_a| \gtrsim 1$, such as the profiles at $\varphi_0 = 34.53°$ ($R_a = 1$) and $35.46°$ ($R_a = -1.1$), are true for the test in Eq. (5).

Identification of isolated MDs is a crucial step in testing the compatibility of structure models to profile asymmetries. Coincidental BC lines of comparable strength (W value) crossing the primary BC line at close positions can compromise the asymmetry analysis, as shown for example in Fig. 7. When the instrument accommodates access to both out-in and in-out excitation geometries, the profiles must present opposite asymmetries. Otherwise, only the one with isolated BC line or with very weak neighbors can be used, as for instance in Fig. 7(b).

A. Refining the model structures

More refined models are obtained by accounting for small changes of electronic charges. In this purpose, the atomic scattering factors for the amino group are writ-

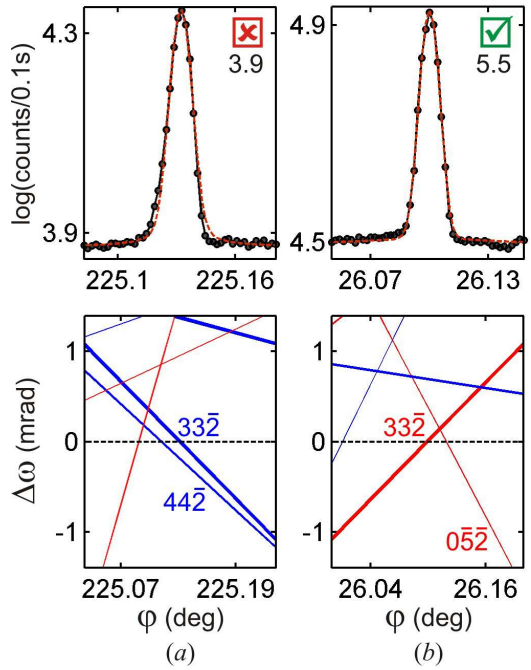

FIG. 7: (a) Out-in and (b) in-out experimental profiles of a same MD case. The H|L asymmetry in (a) is caused by the nearby 44$\bar{2}$ BC line. R_a values are shown below the true/false checkbox for compatible asymmetry with the NH3 model. Horizontal dashed line stands for 26$\bar{1}$ BC line.

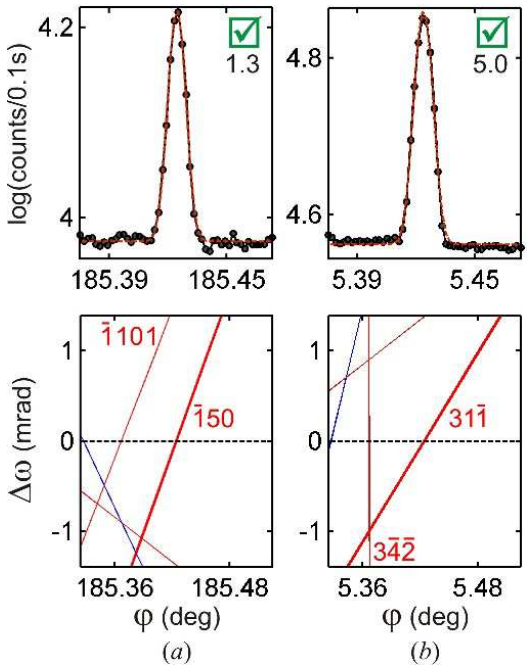

FIG. 8: Experimental profiles and respective $\omega : \varphi$ graphs of most susceptible cases for charge variation in the amino group. R_a values are shown below the true/false checkbox for compatible asymmetry with the NH3 model. Horizontal dashed lines stand for 26$\bar{1}$ BC line.

ten as $f_{\mathrm{N}^{3x-}} = (1-x)f_{\mathrm{N}} + xf_{\mathrm{N}^{3-}}$ for the nitrogen and $f_{\mathrm{H}^{x+}} = (1-x)f_{\mathrm{H}}$ for the hydrogens. $x = 0$ and $x = 1$ are the two extreme situations represented in the NH3 and N3e models, respectively. Phase measurements agree with theoretical phases for $x = 0$. However, by slightly changing x we can have a more accurate idea of how susceptible the phases actually are to electronic charge distribution at the amino group.

For $x = 0.1$, shifts in triplet phases of about $\Delta\Psi = \pm 4°$ would be enough to invert the line profile asymmetry of a few MD peaks of reasonable amplitudes $W > 5\%$; they are indicated as the most susceptible cases in the list at § A 3. However, experimentally we are limited to the peaks with isolated BC line and reliable value of asymmetry ($|R_a| \geq 1$) that are shown in Fig. 8. Their asymmetries are consistent to the NH3 model where $x < 0.1$, which means that hydrogens in the amino group are practically neutral atoms with effective ionic charges smaller than $+0.1e$.

Compatibility of other models have been also verified. For instance, a model with one electron removed from the nitrogen and shared between the oxygens. Atomic scattering factors are for nitrogen N^{+} and oxygen $\mathrm{O}^{0.5-}$ ions, while all other atoms are neutral. When compared to the NH3 model, the MD peaks that could present inversion of asymmetry are exactly the same ones previously analyzed in Fig. 8. Then, there is not evidence to sustain such model. On the other hand, a zwitterion model where the electron from the N^{+} ion is placed at the nearest oxygen O^{-} ion, as indicated in Fig. 1 (inset), seems to be compatible to the data. In comparison to the NH3 model, the discrepancies are listed in Table II and the MD peaks of this list that could be measured are shown in Fig. 9. The phase shifts are very small and can affect only MD cases with Ψ very close to $\pm 90°$, whose asymmetric character are difficult to identify. Although, the four profiles agree with the zwitterion model, the most reliable profile is the one in Fig. 9(c) since there are no nearby BC lines and the asymmetric parameter value $R_a = 0.9$ is close to the detectability limit of asymmetry established in Eq. (4).

B. Radiation damage

By using the multi-axis goniometry, MD peaks on other primary reflections could be measured. Most of the profiles agree with the NH3 model, as those in Figs. 10 (a,b). But, there were two exception that are shown in Figs. 10 (c,d). The MD with primary 261 and secondary $\bar{1}$50 is very susceptible to ionic charges at the amino group, as previously discussed when using primary 26$\bar{1}$, Fig. 8. However, in this case, the asymmetry seen in Fig. 10(c) is clearly of the L|H type, suggesting a higher ionization of the hydrogens in the amino group. Incident beam with a flux of about 30 times higher in this later experiments increases the average number of ionized hydrogens at the intermolecular bonds during data acquisition,

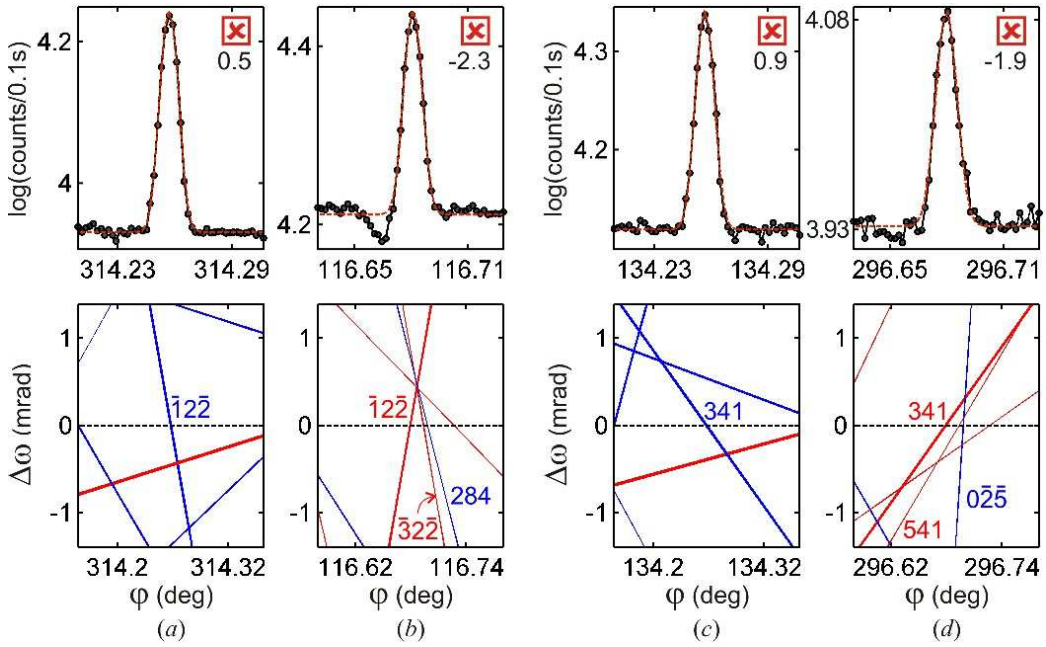

FIG. 9: Experimental profiles and respective $\omega : \varphi$ graphs of most susceptible cases to a zwitterion. R_a values are shown below the true/false checkbox for compatible asymmetry with the NH3 model. Horizontal dashed lines stand for $26\bar{1}$ BC line.

H	$\Psi\,(^\circ)$	$\Psi''\,(^\circ)$	$W(\%)$	$\varphi_{\rm oi}\,(^\circ)$	$\varphi_{\rm io}\,(^\circ)$
$\bar{1}2\bar{2}$	−88.8	−90.7	18	314.258	116.679
341	−88.8	−90.7	18	134.258	296.679
$\bar{4}71$	91.3	89.9	8	47.780	157.278
$6\bar{1}\bar{2}$	91.3	89.9	8	227.780	337.278
$\bar{1}2\bar{3}$	90.9	88.6	8	310.281	100.009
342	90.9	88.6	8	130.281	280.009
$3\bar{4}\bar{2}$	90.9	89.0	6	232.542	5.367
$\bar{1}101$	90.9	89.0	6	52.542	185.367

TABLE II: MD cases in which $\cos(\Psi)\cos(\Psi'') < 0$, ordered by their relative amplitude W. Model structures NH3 (Ψ) and zwitterion (Ψ'') of D-alanine. Secondary H reflections diffracting at azimuth $\varphi_{\rm oi}$ (out-in) and $\varphi_{\rm io}$ (in-out). Primary reflection $G = 26\bar{1}$. X-rays of 10 keV.

which can explain the observed asymmetry in Fig. 10(c). On the other hand, profile asymmetries with primary 080 are not susceptible to the model structures discussed in this work. The MD profile observed in Fig. 10(d) has poor sensitivity to the triplet phase due to weak Umweganregung and strong Aufhellung components[12,23]. A situation that often occurs when combining strong H secondary reflection, such as 125, with weak $G - H$ coupling reflection, such as $\bar{1}6\bar{5}$.

VII. CONCLUSIONS

Sensitivity of X-ray phase measurements has been tested in detecting electronic charge distribution in D-alanine. It clearly shown that the hydrogens in the amino group are practically neutral atoms with null or very small effective ionic charges. Besides a model where all atoms are neutral, the only other model that can agree with the whole data set of MD profiles asymmetries is the zwitterion model where a electron from the nitrogen orbitals goes to the nearest oxygen. In this case, intermolecular forces stabilizing D-alanine crystal at ambient pressure can be also van der Waals forces and not only hydrogen bonds. There are several experimental and data analysis procedures developed during this work that are crucial for practical applications of phase measurements: using of graphical indexing, establishing a parameter of asymmetry, comparison of triplet phases from model structures, and certification of the primary reflection by the crystal rotating method.

Acknowledgments

Acknowledgments are due to the Brazilian funding agencies CNPq (Grant Nos. 306982/2012-9 and 452031/20150), FAPESP (Grant Nos. 2012/01367-2, 12/15858-8, 14/08819-1, 14/21284-0, and 16/11812-4), Diamond Light Source (proposal MT11922), Brazilian Synchrotron Light Source (proposals 17063, 18011, and 19018).

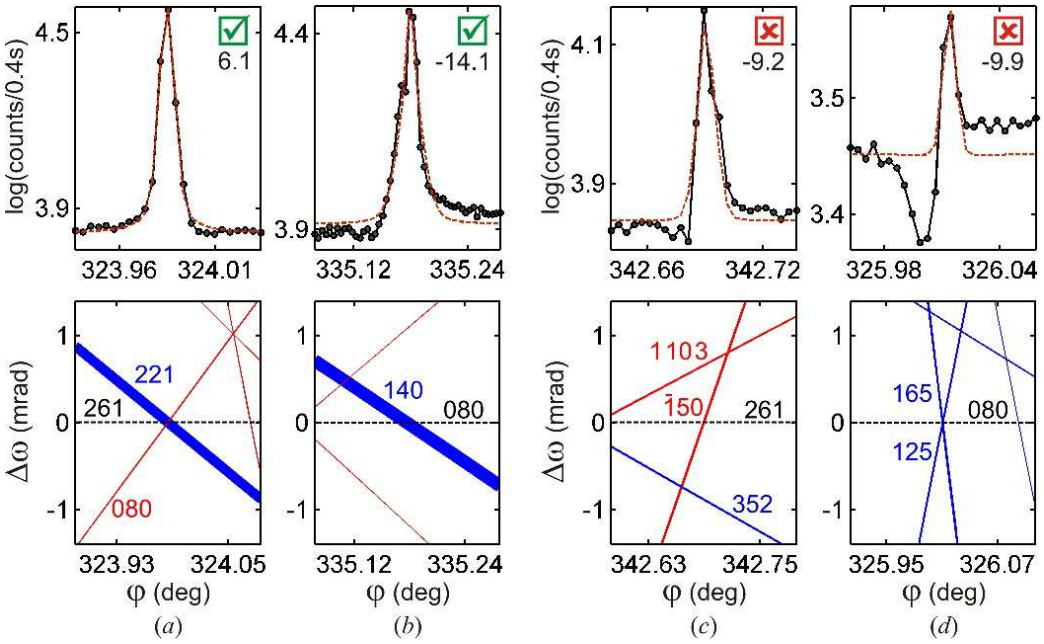

FIG. 10: Experimental profiles and respective $\omega : \varphi$ graphs of a few MD peaks measured using multi-axis goniometry for primary (a,c) 261 and (b,d) 080. R_a values are shown below the true/false checkbox for compatible asymmetry with the NH3 model.

* corresponding author: morelhao@if.usp.br

[1] Z. G. Amirkhanyan, C. M. R. Remédios, Y. P. Mascarenhas, and S. L. Morelhão, J. Appl. Cryst. **47**, 160 (2014).

[2] S. L. Morelhão, C. M. R. Remédios, R. O. Freitas, and A. O. dos Santos, J. Appl. Cryst. **44**, 93 (2011).

[3] S. L. Morelhão, Z. G. Amirkhanyan, and C. M. R. Remédios, Acta Cryst. A **71**, 291 (2015).

[4] J. Z. Domagała, S. L. Morelhão, M. Sarzyński, M. Maździarz, P. Dłużewski, and M. Leszczyński, J. Appl. Cryst. **49**, 798 (2016).

[5] A. G. A. Nisbet, G. Beutier, F. Fabrizi, B. Moser, and S. P. Collins, Acta Cryst. A **71**, 20 (2015).

[6] M. Renninger, Z. Kristallogr. **97**, 107 (1937).

[7] M. Hart and A. R. Lang, Phys. Rev. Lett. **7**, 120 (1961).

[8] B. Post, Phys. Rev. Lett **39**, 760 (1977).

[9] L. D. Chapman, D. R. Yoder, and R. Colella, Phys. Rev. Lett **46**, 1578 (1981).

[10] H. J. Juretschke, Phys. Rev. Lett. **48**, 1487 (1982).

[11] S.-L. Chang, Chinese J. Phys. **35**, 896 (1997).

[12] E. Weckert and K. Hümmer, Acta Cryst. A **53**, 108 (1997).

[13] S. L. Morelhão and S. Kycia, Phys. Rev. Lett. **89**, 015501 (2002).

[14] Q. Shen, I. S. Elfimov, P. Fanwick, Y. Tokura, T. Kimura, K. Finkelstein, R. Colella, and G. A. Sawatzky, Phys. Rev. Lett. **96**, 246405 (2006).

[15] E. V. Boldyreva, in *Models, Mysteries, and Magic of Molecules*, edited by J. C. A. Boeyens and J. F. Ogilvie (Springer Verlag, 2007), chap. 7, pp. 196–194.

[16] N. P. Funnell, A. Dawson, D. Francis, A. R. Lennie, W. G. Marshall, S. A. Moggach, J. E. Warren, and S. Parsons, CrystEngComm **12**, 2573 (2010).

[17] J. W. Moore, C. L. Stanitski, and P. C. Jurs, *Chemistry: The Molecular Science* (Brooks Cole, 2011).

[18] C. C. Wilson, D. Myles, M. Ghosh, L. N. Johnson, and W. Wang, New J. Chem. **29**, 1318 (2005).

[19] P. J. Brown, A. G. Fox, E. N. Maslen, M. A. O'Keefe, and B. T. M. Willis, in *International Tables for Crystallography C*, edited by E. Prince (IUCr, 2006), chap. 6.1, pp. 554–595.

[20] R. O. Freitas, T. E. Lamas, A. A. Quivy, and S. L. Morelhão, Phys. Stat. Sol. A **204**, 2548 (2007).

[21] Y. P. Stetsko, H. J. Juretschke, Y. S. Huang, C. K. C. C. H. Chao, and S. L. Chang, Acta Cryst. A **56**, 394 (2000).

[22] S. L. Morelhão and L. H. Avanci, Acta Cryst. A **57**, 192 (2001).

[23] E. Rossmanith, J. Appl. Cryst. **32**, 355 (1999).

[24] S. L. Morelhão, *Computer Simulation Tools for X-ray Analysis* (Springer International Publishing, 2016), `rotcrystmethod.m` routine, p. 272.

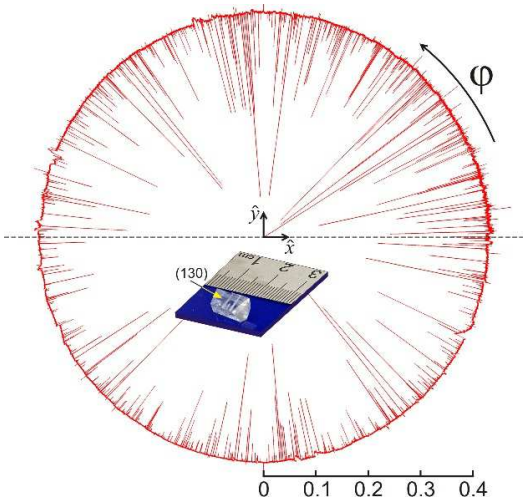

FIG. 11: Complete Renninger scan of reflection $26\bar{1}$ in polar plot: $x = -\log(I/I_{max})\cos\varphi$ and $y = -\log(I/I_{max})\sin\varphi$. $I_{max} = 1.8 \times 10^5$ counts/0.1s. X-rays of 10 keV, σ polarization. Reference direction ($\varphi = 0$): c axis in the incident plane pointing downstream. Sense of sample rotation: clockwise with the diffraction vector pointing to the observer. Inset: used sample, (130) face exposed to X-rays.

Appendix A: Supplemental Information

1. Azimuthal scanning with a single goniometer axis

The full Renninger scan of the $26\bar{1}$ reflection shown in Fig. 11 is composed of 72 uninterrupted φ scans. At the first point of each scan, the primary reflection has been centered at its rocking-curve (FWHM of 0.07 mrad). The maximum drift of the rocking-curves center as a function of φ was 0.2 mrad. Only in Fig. 11, smooth variations of the baseline intensity have been flattened for the sake of visualization of the 180° symmetry of the data, although peak intensities are different since the (130) entrance surface normal direction is not the one aligned to the rotation axis.

2. Physical alignment of primary reflection by using the rotating crystal method

With an area detector (the pilatus 100K in our case) attached to the 2θ arm of the single crystal diffractometer, 2D array indices $m_c n_c$ of the reference pixel receiving most of the direct beam ($2\theta = 0$) are identified. After fixing the sample in a goniometer head that has arcs for orientation correction, placing the area detector at a distance D from the sample, and moving the detector arm to a desired 2θ value, the φ axis is spun by 360° while the detector acquires images at the rate of one frame per degree of rotation. Diffraction spots at pixels of indices mn correspond to reflections with scattering angles

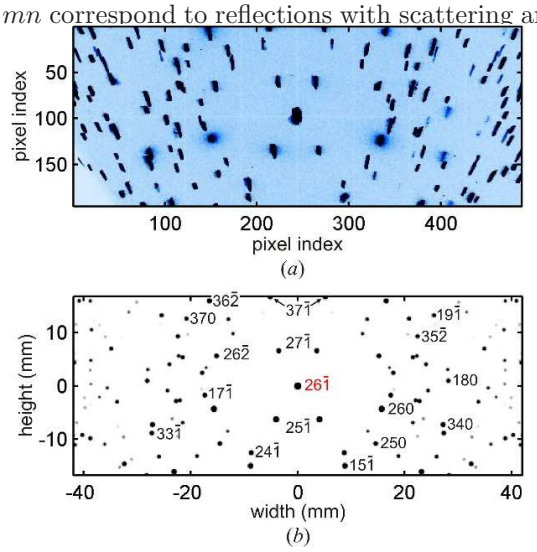

FIG. 12: (a) Diffraction spots on detector area collected in a 360° spin of the sample around diffraction vector of reflection $26\bar{1}$. Sample-detector distance is 74.7 mm. X-rays of 10 keV, σ polarization. (b) Indexing of diffraction spots by simulation of the rotating crystal method[24]. Area detector width at horizontal direction.

$2\theta_{mn} = \cos^{-1}(\hat{R}\cdot\hat{z})$ where $\boldsymbol{R} = |\boldsymbol{R}|\hat{R} = \boldsymbol{R}_c + \boldsymbol{r}_d$, $\boldsymbol{R}_c = D[\sin(2\theta)\hat{x} + \cos(2\theta)\hat{z}]$, $\boldsymbol{r}_d = -(n-n_c)p\hat{x}_d + (m-m_c)p\hat{y}_d$, $\hat{x}_d = \cos(2\theta)\hat{x} - \sin(2\theta)\hat{z}$, and $\hat{y}_d = \hat{y}$. In the lab frame, $\hat{z}$ is along the direct beam, $\hat{x}$ is vertical, $\hat{y}$ is horizontal. Pixel size for the used detector is $p = 0.172$ mm.

A diffraction spot with scattering angle close to that of the desired primary reflection is selected and aligned to the φ axis. By using as input pixel indices mn and azimuth φ_{mn} of a spot, a script suitable to the used diffractometer was written to provide the values by which each arc has to be corrected. A new spin of the rotation axis is then carried out to confirm that the aligned reflection is in fact the desired one, as shown in Fig. 12 for the $26\bar{1}$ reflection.

3. List of triplet phases susceptible to model structures

H	Ψ (°)	Ψ' (°)	W(%)	$\varphi_{\rm oi}$ (°)	$\varphi_{\rm io}$ (°)
040	−98.1	−60.4	100	12.199	212.730
$22\bar{1}$	−98.1	−60.4	100	192.199	32.730
$\bar{1}31$	72.9	111.1	31	45.132	206.099
$33\bar{2}$	72.9	111.1	31	225.132	26.099
110	−102.3	−65.4	29	130.286	357.040
$15\bar{1}$	−102.3	−65.4	29	310.286	177.040
220	75.0	112.3	28	143.710	343.615
$04\bar{1}$	75.0	112.3	28	323.710	163.615
012	−116.0	−79.5	25	98.710	246.456
$25\bar{3}$	−116.0	−79.5	25	278.710	66.456
$1\bar{2}2$	79.9	112.8	23	151.438	279.499
$18\bar{3}$	79.9	112.8	23	331.438	99.499
$2\bar{2}0$	75.3	112.5	23	188.775	346.556
$08\bar{1}$	75.3	112.5	23	8.775	166.556
$1\bar{2}\bar{2}$	79.0	118.0	23	249.286	43.466
181	79.0	118.0	23	69.286	223.466
$\bar{1}50^{\dagger}$	89.8	125.5	19	15.689	185.424
$31\bar{1}^{\dagger}$	89.8	125.5	19	195.689	5.424
$2\bar{6}0$	75.5	112.7	19	221.416	331.212
$0\,12\,\bar{1}$	75.5	112.7	19	41.416	151.212
020	79.1	118.8	18	1.584	223.346
$24\bar{1}$	79.1	118.8	18	181.584	43.346
$\bar{1}1\bar{3}^{\dagger}$	89.7	130.9	17	306.476	93.272
$352^{\dagger}$	89.7	130.9	17	126.476	273.272
223	73.1	107.5	17	126.720	267.779
$04\bar{4}$	73.1	107.5	17	306.720	87.779
221	−111.9	−75.2	17	126.354	304.583
$04\bar{2}$	−111.9	−75.2	17	306.354	124.583
$22\bar{3}$	−102.6	−62.6	16	256.833	54.872
042	−102.6	−62.6	16	76.833	234.872
$\bar{1}\bar{5}\bar{1}$	78.0	114.8	14	333.637	351.023
$3\,11\,0$	78.0	114.8	14	153.637	171.023
241	71.4	106.1	13	108.155	286.344
$02\bar{2}$	71.4	106.1	13	288.155	106.344
$\bar{3}9\bar{1}$	62.4	100.2	13	23.392	146.181
$5\bar{3}0$	62.4	100.2	13	203.392	326.181
$0\bar{4}3$	71.8	109.0	13	178.286	228.492
$2\,10\,\bar{4}$	71.8	109.0	13	358.286	48.492
$\bar{3}91$	83.0	120.5	13	47.717	166.996
$5\bar{3}\bar{2}$	83.0	120.5	13	227.717	346.996
$19\bar{1}$	−121.8	−85.0	13	27.688	164.940
$1\bar{3}0$	−121.8	−85.0	13	207.688	344.940
$\bar{1}91$	−95.5	−57.5	12	49.364	189.562
$3\bar{3}\bar{2}$	−95.5	−57.5	12	229.364	9.562
$\bar{2}\bar{2}\bar{1}$	82.1	119.9	12	349.250	81.687
480	82.1	119.9	12	169.250	261.687
$32\bar{2}$	−100.9	−59.0	12	222.921	24.966
$\bar{1}41$	−100.9	−59.0	12	42.921	204.966
$43\bar{3}$	56.7	94.8	12	244.698	13.819
$\bar{2}32$	56.7	94.8	12	64.698	193.819

TABLE III: MD cases in which $\cos(\Psi)\cos(\Psi') < 0$, ordered by their relative amplitude W. Model structures NH3 (Ψ) and N3e (Ψ') of D-alanine. Secondary H reflections diffracting at azimuth $\varphi_{\rm oi}$ (out-in) and $\varphi_{\rm io}$ (in-out). Primary reflection $G = 26\bar{1}$. X-rays of 10 keV. †Most susceptible cases, see text.

H	Ψ (°)	Ψ' (°)	W(%)	$\varphi_{\rm oi}$ (°)	$\varphi_{\rm io}$ (°)
$\bar{1}1\bar{4}$	−121.3	−80.9	11	308.399	82.046
353	−121.3	−80.9	11	128.399	262.046
$2\bar{2}1$	82.1	119.9	11	169.397	317.928
$08\bar{2}$	82.1	119.9	11	349.397	137.928
$2\bar{2}\bar{3}$	73.2	107.7	11	251.254	34.538
082	73.2	107.7	11	71.254	214.538
$1\bar{5}\bar{1}$	−107.5	−70.0	11	243.691	1.598
1 11 0	−107.5	−70.0	11	63.691	181.598
$\bar{1}32$	−115.7	−71.6	11	70.307	215.484
$33\bar{3}$	−115.7	−71.6	11	250.307	35.484
$\bar{3}52$	72.6	109.2	10	59.499	177.530
$51\bar{3}$	72.6	109.2	10	239.499	357.530
$1\bar{5}1$	−122.2	−85.5	10	209.240	300.765
1 11 $\bar{2}$	−122.2	−85.5	10	29.240	120.765
033	57.4	93.0	10	96.718	235.527
$23\bar{4}$	57.4	93.0	10	276.718	55.527
$30\bar{1}$	−105.1	−67.9	10	199.506	4.389
$\bar{1}60$	−105.1	−67.9	10	19.506	184.389
$303^{\dagger}$	88.9	125.2	10	150.154	280.783
$\bar{1}6\bar{4}^{\dagger}$	88.9	125.2	10	330.154	100.783
044	71.2	109.0	9	104.820	227.425
$22\bar{5}$	71.2	109.0	9	284.820	47.425
$0\bar{4}2$	56.5	93.2	9	195.787	235.150
2 10 $\bar{3}$	56.5	93.2	9	15.787	55.150
$\bar{2}91$	56.0	90.9	9	46.876	178.054
$4\bar{3}\bar{2}$	56.0	90.9	9	226.876	358.054
$47\bar{1}$	−111.1	−73.8	9	210.734	294.471
$\bar{2}\bar{1}0$	−111.1	−73.8	9	30.734	114.471
113	78.0	115.7	9	120.854	258.238
$15\bar{4}$	78.0	115.7	9	300.854	78.238
$\bar{1}22$	−108.2	−71.8	9	76.270	216.482
$34\bar{3}$	−108.2	−71.8	9	256.270	36.482
$4\bar{7}\bar{1}$	−98.5	−61.4	9	230.598	334.460
$\bar{2}$ 13 0	−98.5	−61.4	9	50.598	154.460
$\bar{3}1\bar{1}$	61.1	99.7	9	3.599	123.727
550	61.1	99.7	9	183.599	303.727
$06\bar{1}$	−104.9	−67.6	9	349.121	169.121
200	−104.9	−67.6	9	169.121	349.121
$\bar{4}10$	71.0	107.4	8	36.159	127.273
$65\bar{1}$	71.0	107.4	8	216.159	307.273
$0\bar{4}\bar{5}$	79.1	116.3	8	297.261	39.924
2 10 4	79.1	116.3	8	117.261	219.924
$10\bar{5}^{\dagger}$	88.9	125.3	8	288.312	52.335
$164^{\dagger}$	88.9	125.3	8	108.312	232.335
$\bar{1}5\bar{1}$	−107.1	−69.5	8	350.045	159.960
310	−107.1	−69.5	8	170.045	339.960
$\bar{2}2\bar{1}$	−111.9	−75.2	8	349.629	137.696
440	−111.9	−75.2	8	169.629	317.696
$2\bar{5}\bar{3}$	−93.8	−55.8	8	256.498	17.602
0 11 2	−93.8	−55.8	8	76.498	197.602
291	−98.3	−62.0	8	93.276	227.881
$0\bar{3}\bar{2}$	−98.3	−62.0	8	273.276	47.881
$29\bar{3}$	−118.5	−81.1	8	347.523	65.396
$0\bar{3}2$	−118.5	−81.1	8	167.523	245.396

TABLE IV: Continuation of Table III.

H	Ψ (°)	Ψ' (°)	W(%)	$\varphi_{\rm oi}$ (°)	$\varphi_{\rm io}$ (°)
$\bar{3}5\bar{3}$	−115.4	−76.2	7	350.843	115.079
512	−115.4	−76.2	7	170.843	295.079
2 10 0	−104.9	−67.7	7	88.465	197.326
$04\bar{1}$	−104.9	−67.7	7	268.465	17.326
$2\bar{2}\bar{1}$	68.5	105.5	7	212.730	12.199
080	68.5	105.5	7	32.730	192.199
$1\bar{1}3$	−119.2	−83.7	7	137.959	261.789
$17\bar{4}$	−119.2	−83.7	7	317.959	81.789
$\bar{4}1\bar{2}$	81.6	120.7	7	4.144	105.511
651	81.6	120.7	7	184.144	285.511
452	−114.6	−83.7	7	144.342	277.693
$\bar{2}1\bar{3}$	−114.6	−83.7	7	324.342	97.693
$2\bar{9}1$	−111.3	−73.2	7	243.455	288.416
$0\,15\,\bar{2}$	−111.3	−73.2	7	63.455	108.416
$2\bar{9}\bar{3}^{\dagger}$	−91.1	−54.0	7	272.849	351.002
$0\,15\,2^{\dagger}$	−91.1	−54.0	7	92.849	171.002
$2\bar{2}3$	77.5	117.5	7	155.071	275.866
$08\bar{4}$	77.5	117.5	7	335.071	95.866
$\bar{1}\bar{1}3$	−100.3	−61.7	7	123.612	213.573
$37\bar{4}$	−100.3	−61.7	7	303.612	33.573
$02\bar{1}$	−105.2	−68.0	7	292.536	138.401
240	−105.2	−68.0	7	112.536	318.401
$\bar{4}7\bar{1}$	81.5	118.7	7	23.451	138.333
$6\bar{1}0$	81.5	118.7	7	203.451	318.333
151	68.2	95.6	6	72.265	252.396
$11\bar{2}$	68.2	95.6	6	252.265	72.396
$\bar{4}80$	−100.0	−62.3	6	36.955	148.779
$6\bar{2}\bar{1}$	−100.0	−62.3	6	216.955	328.779
$5\bar{3}\bar{1}$	−111.3	−72.4	6	214.859	337.769
$\bar{3}90$	−111.3	−72.4	6	34.859	157.769
$0\bar{1}\bar{5}$	−112.3	−75.1	6	297.451	56.389
274	−112.3	−75.1	6	117.451	236.389
$2\bar{5}3$	−115.9	−79.4	6	183.114	272.406
$0\,11\,\bar{4}$	−115.9	−79.4	6	3.114	92.406
$3\bar{5}\bar{3}$	65.1	103.3	6	249.389	8.130
$\bar{1}\,11\,2$	65.1	103.3	6	69.389	188.130
$0\bar{2}3$	−96.5	−59.2	6	142.757	239.697
$28\bar{4}$	−96.5	−59.2	6	322.757	59.697
$3\bar{1}\bar{1}$	60.6	99.2	6	203.632	2.468
$\bar{1}70$	60.6	99.2	6	23.632	182.468
$47\bar{2}$	83.9	115.0	6	264.522	320.407
$\bar{2}\bar{1}1$	83.9	115.0	6	84.522	140.407
171	−123.0	−79.9	6	68.727	232.517
$1\bar{1}\bar{2}$	−123.0	−79.9	6	248.727	52.517
063	75.8	113.0	6	86.901	224.804
$20\bar{4}$	75.8	113.0	6	266.901	44.804
$3\bar{9}\bar{1}$	−117.8	−80.0	6	246.331	328.382
$\bar{1}\,15\,0$	−117.8	−80.0	6	66.331	148.382
$\bar{1}\bar{1}4$	64.5	103.9	6	132.753	210.450
$37\bar{5}$	64.5	103.9	6	312.753	30.450
$3\bar{7}1$	−97.0	−63.7	6	213.368	309.085
$\bar{1}\,13\,\bar{2}$	−97.0	−63.7	6	33.368	129.085

TABLE V: Continuation of Table IV.